Design, Development, and Testing of Polymeric Microblades: A Novel Design of Microneedles for Biomedical Applications

Vahid Ebrahiminejad and Zahra Faraji Rad*

Conventional microneedles (MNs) are designed as an array of micrometer-sized projections that can painlessly penetrate the skin. Fabrication of MN arrays can be costly and time-consuming; additionally, full penetration of an array of MNs with ten to thousands of projections into the skin may not be achievable. This paper reports a new design of MNs known as microblades (MBs) which consist of a singular microstructure. The single integrated design of the MBs reduces the fabrication cost and time, facilitates more effective penetration, and may pave the way for the scale-up manufacturing of MN devices. Different designs of MBs are fabricated by two-photon polymerization technique, followed by polydimethylsiloxane micromolding and soft embossing to create replicas. The mechanical integrity of the designs is determined by a series of compression tests. Skin insertion and drug diffusion studies are conducted using a custom-made applicator to insert the MBs into the porcine abdominal skin to demonstrate delivery of fluorescein tracer. MBs insertion and penetration capabilities and the diffusion of a model drug into a multi-layered human skin are demonstrated using finite element analysis and 3D diffusion models. The results demonstrate the functional capabilities of the MBs as an alternative to MN arrays.

1. Introduction

Recent developments in micro-electromechanical systems (MEMS) have paved the way for the advancement of microscale devices, especially in biomedical research. One of these remarkable research developments is the application of microneedles (MNs) as an alternative to conventional hypodermic needles.[1] Traditional hypodermic needles are invasive, stimulate pain, produce hazardous wastes, and need trained medical staff for administration. MNs are minimally invasive devices which enable painless administration of therapeutic molecules and

sampling biomarkers such as interstitial fluid for point-of-care (POC) diagnostics by bypassing the stratum corneum (SC) barrier of the skin.[2,3] The COVID-19 pandemic, more than any other time, highlights the necessity for new methods to overcome the issues associated with mass vaccination, distribution, logistics, drug delivery, and inexpensive and rapid POC testing.

MNs are generally made from silicon, metals, ceramics, silica glass, carbohydrates, and polymers and are studied for vaccination, drug delivery, and diagnostics purposes.[4] Based on the application, MNs are classified into solid, coated, dissolving, hollow or open-channel, and hydrogel-forming structures.[5] MNs are manufactured using methods such as wet etching, reactive ion etching (RIE), deep reactive ion etching (DRIE), lithography, micromolding, injection molding, laser drilling, 3D printing, and two-photon polymerization (2PP).[4–9] The geometries consist of cylindrical, conical, pyramidal, or prismatic shapes of miniaturized needles arranged in an array. Even though significant research has been done on MN technologies, not all geometries and materials can be fully inserted into the skin, which limits the MN arrays' functionality.

Although traditional MN designs are promising tools for transdermal drug delivery and diagnostics, some issues remain during fabrication, insertion, and testing. For instance, scale-up fabrication of these designs is still challenging due to the need to manufacture high-density arrays. Current conventional manufacturing techniques such as RIE, DRIE, lithography, and laser ablation are expensive multistage methods that are limited to select materials and geometrical designs.[10,11] Additive manufacturing methods such as stereolithography, 2PP, and micromolding are more flexible, cost-effective, and involve simpler processes; however, they are deemed as more time-consuming methods.[12,13] Process modification and optimization may improve the fabrication time and the accuracy of these techniques.[14,15]

MN devices require adequate strength to penetrate the skin while maintaining mechanical integrity. Mechanical failures are usually due to buckling failure during normal insertion or transverse bending failure due to the excessive lateral loads caused by skin natural elasticity and irregular topology.[4] MN mechanical integrity primarily depends on the geometrical shape, material selection,[16–18] and manufacturing process.[19,20] The MN geometrical aspects affecting mechanical strength

V. Ebrahiminejad, Z. Faraji Rad
School of Engineering
University of Southern Queensland
Springfield Central, QLD 4300, Australia
E-mail: zahra.farajirad@usq.edu.au

The ORCID identification number(s) for the author(s) of this article can be found under https://doi.org/10.1002/admi.202201115.

are correlated with MN length,[16] aspect ratio (the ratio of the length to width),[21,22] base diameter,[16,21] base vertices,[23] wall thickness, and tip area.[24] Thereby, geometrical optimization plays a remarkable role in improving the device's stability, performance, and insertion safety. Nondissolving solid MNs possess higher mechanical strength; however, only a limited amount of drugs can be loaded on them.[25,26] For POC diagnostics, solid MNs should also be accompanied by a secondary device to enable sample extraction and storage.[27] Hollow MNs with microscale inner channels allow for increased drug delivery and sampling; though, channel clogging and early fracture due to thinner walls still pose a risk during insertion.[26] Furthermore, once MN arrays are applied to the skin, partial penetration causes the "bed of nails" effect where outer-most MNs locally stretch the skin, causing the inner MNs to only partially or not at all penetrate an already stretched skin[28] which is one the most limiting phenomena in effective MN array penetration.

In addition, the mechanics of MN penetration into the skin is equally important to the MN's mechanical strength to enable a safe and effective insertion. Insertion characteristics assist in determining the safety margin (SM), known as the ratio of MN's fracture force to the skin's insertion force.[24] The SM should be maximized and be greater than unity for an MN to be mechanically safe.[16] During the MN insertion, the applied force linearly increases before reaching a peak force, the so-called insertion force, prior to breaking the skin's top layer (SC).[2,29] Reduction in the insertion force can directly influence safety by improving the SM. In addition, reducing the force required to insert into the skin reduces the overall compression of the skin, which minimizes tissue damage and the amount of pain experienced by patients.[26] The application method is another approach to improve insertion safety and effectiveness. In general, insertions can be made via a pressing force through manual thumb force or using an applicator. Applicators can be used to generate a controlled pressing force or impact force by predetermining the impact velocity or energy.[30] The conventional method of MN thumb pressing is known to have less force uniformity and reproducibility,[31] which can lead to early breakage or bending of MNs during insertion. Studies by Ranamukhaarachchi and Stoeber and Olatunji et al. showed the effect of increasing impact velocity, which reduced the insertion force and improved the SM ratio.[2,32] These studies indicated that an increase of impact velocity from 0 to 4.3 m s^{-1} for metallic hollow MNs reduced the insertion force from 0.88 to 0.37 N.

The aforementioned issues can be minimized by introducing new designs and mechanically stable microdevices capable of transferring different molecular size drugs and sampling biofluids with a single mechanically sturdy structure. In this study, we report a new design of MN called a microblade (MB) with the futuristic potential for drug delivery. Our recently patented MB structure incorporates a solid design with multiple side channels and reservoirs to enable effective penetration into the skin for different applications as required.[33] Similar to MNs, MBs require sufficient mechanical strength to endure the potential failure risks during insertion into the skin. This work aims to design, fabricate, and test the mechanical strength of MBs with different geometrical features. This is followed by in vitro insertion tests of the MBs using a custom-made prototype applicator with adjustable impact velocity and pressing force. The MB insertion mechanics, such as insertion force and penetration depth on the skin subjects, were modeled and simulated with the explicit dynamics method of finite element analysis (FEA). Additionally, the diffusion and concentration of the model drug were investigated and compared for each individual MB using experimental and simulation approaches.

2. Experimental Section

2.1. Design of Open-Channel MBs

The geometrical design of the five MBs presented in this study was generated using SolidWorks (Dassault Systems SolidWorks Corporation, Concord, NH, USA). The MB height was 900 µm, with six 50 µm diameter microfluidic channels on each side to enable the transfer of large cells and drug contents. The channels were connected to two microfluidic reservoirs at the sides. The five MBs presented geometrically differed based on the blade angle and the eccentricity level with respect to the center. While the first three models incorporated 90°, 120°, and 180° (square shape) blade angles, in the other two models, the MB tips were located half- and full-eccentric with respect to the centers (**Figure 1**). **Table 1** shows the schematic design of each MB (Types 1–5) and summarizes their geometrical features.

2.2. Fabrication of Master Microblades using 2PP

Five individual open-channel master MBs were printed by 2PP using the commercial Nanoscribe Photonic Professional GT
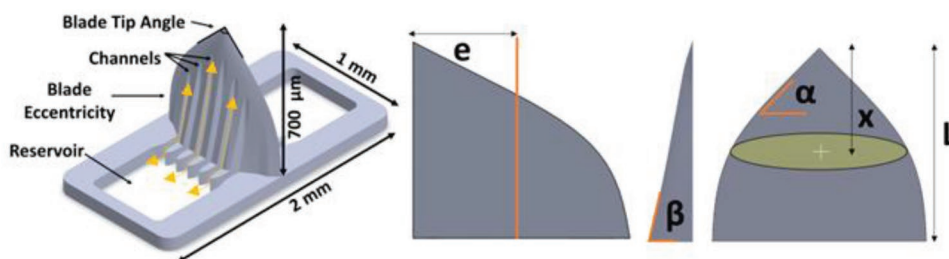

Figure 1. An overall view of the features and dimensions associated with the MB designs. Each MB has a 1×2 mm^2 base plate, including two side reservoirs connected to multiple channels. MBs have a 0.9 mm length with various tip angles and eccentricity. Parameters including eccentricity (e), side angles (α, β), distance to the MB tip (x), and overall length (L) are defined for mathematical models.

**ADVANCED
SCIENCE NEWS**

www.advancedsciencenews.com

**ADVANCED
MATERIALS
INTERFACES**

www.advmatinterfaces.de

Table 1. Geometrical features and dimensions of five different types of MBs.

Type	Blade angle [°]	Height [µm]	Eccentricity	Schematic
1	90	900	Concentric	
2	120	900	Concentric	
3	180	900	Concentric	
4	60	900	Full-eccentric	
5	90	900	Half-eccentric	

system (Nanoscribe GmbH, Karlsruhe, Germany). The system was provided with a pulsed erbium-doped femtosecond fiber laser source with a center wavelength of 780 nm for exposing the photosensitive materials. The 3D CAD models were imported to Nanoscribe's Describe software for adjusting different parameters and generating general writing language (GWL) codes required for printing. The GWL codes arranged all the parameters to be applied during the printing and specified the paths followed by the laser focus inside the photoresist.

The model structures were printed with laser power of 100 mW, scanning speed of 100 mm s^{-1}, and 1 µm fixed slicing distance. Triangular scaffolds with a wall spacing of 20 µm were selected for scaffolding. Before printing, each MB was split into blocks of 285 µm × 285 µm × 285 µm (XYZ) with a shear angle of 0°. The GWL codes were adjusted to print multiple MB structures on the same substrate to reduce fabrication time. This code adjustment enabled the fabrication of MB structures by controlling the stage movements through X and Y directions, followed by the movement in the Z-direction to return the laser to the interface position. Additionally, the code redefined the interface between the laser and the substrate. This enabled printing of all MBs simultaneously without delamination from the substrate (Figure S1, Supporting Information).

The negative-tone IP-S photoresist (Nanoscribe GmbH, Karlsruhe, Germany) was used for printing the MBs. A drop of the photoresist was drop cast on the conductive side of the indium tin oxide (ITO) coated glass slide and placed inside the system. To initiate the print process, the final GWL file containing all the specifications of the print was loaded to the NanoWrite software (NanoScribe GmbH, Karlsruhe, Germany) connected to the NanoScribe system. The laser beam focused into the photoresist using a × 25 magnification objective and NA of 0.8. To ensure the final polymerized MBs were fully fixed to the supporting substrate, the MBs were printed with 0.6 µm overlap into the substrate. The MBs were written in the galvo scan mode in XY directions, while the piezo offsetting mode was used for offsetting in the Z-direction. After polymerization, the printed samples were developed in a propylene glycol monomethyl ether acetate (PGMEA) bath for 10 min, rinsed for 2 min in isopropyl alcohol (IPA), and finally air-dried (Figure S2, Supporting Information).

2.3. Casting of Negative PDMS Mold

Negative molds of master MBs were made using polydimethylsiloxane (PDMS) (SYLGARD 184 Silicone Elastomer Kit, Dow Corning, Midland, MI, USA). PDMS solution with a 1:10 curing agent/base ratio was mixed and degassed in a planetary mixer to remove air bubbles. The solution was poured on the MB masters in a petri dish and cured inside a laboratory oven at 80 °C for 2 h. The soft negative PDMS mold was then peeled off from the masters for replication (**Figure 2**a).

2.4. Fabrication of Polymeric MBs using PDMS Mold and Soft Embossing

MB replicas were produced using the soft embossing process. A rheometer (TA Instruments, New Castle, USA) was used to replicate thermoplastic MBs using the negative PDMS mold. A total of ten pellets (two pellets per MB replica) of thermoplastic material (cyclo-olefin polymer, Zeonor 1060R) were mounted onto the PDMS cavities and placed in-between two 40 mm diameter stainless steel plates inside the rhemoter's chamber. The temperature inside the chamber was set to 163 °C, which is 63 °C above the glass transition temperature of the thermoplastic (T_g = 100 °C), to facilitate the flow of low viscous thermoplastic polymer into the mold cavities. While the thermoplastic material was melting, the lower plate was kept fixed, and the upper plate lowered as a function of time and limited to the maximum of 30 ± 5 N axial force. During the embossing process, the upper plate's downward displacement reduced nonlinearly from 100 to 25 µm per interval over the course of 1 h until the upper plate reached 700 µm above the surface of the PDMS mold. The chamber temperature was then reduced to 10 °C for 15 min to allow solidification of the replicas before demolding. Once solidified, the replicas were peeled off from the negative PDMS mold (Figure 2b). The PDMS mold was used several times (>20 cycles) with no defects such as cracks or deformation forming on the mold.

2.5. Mechanical Strength Test of MB Replicas

A series of compression tests were conducted at two different speeds to study the mechanical strength and integrity of the MBs. Five MB replicas were tested using the axial compression test module of the TRIOS package linked to the rheometer used for the soft embossing process. Each MB replica was placed on the lower disk of the rheometer using double-sided tape while the upper plate was lowered at speeds of 1 and 25 µm s^{-1}. The software was programmed to initiate from a predefined distance from the MB tip and lowered by 400 µm. During the test, force and displacement data were recorded to plot the mechanical behavior of individual MBs. The data were
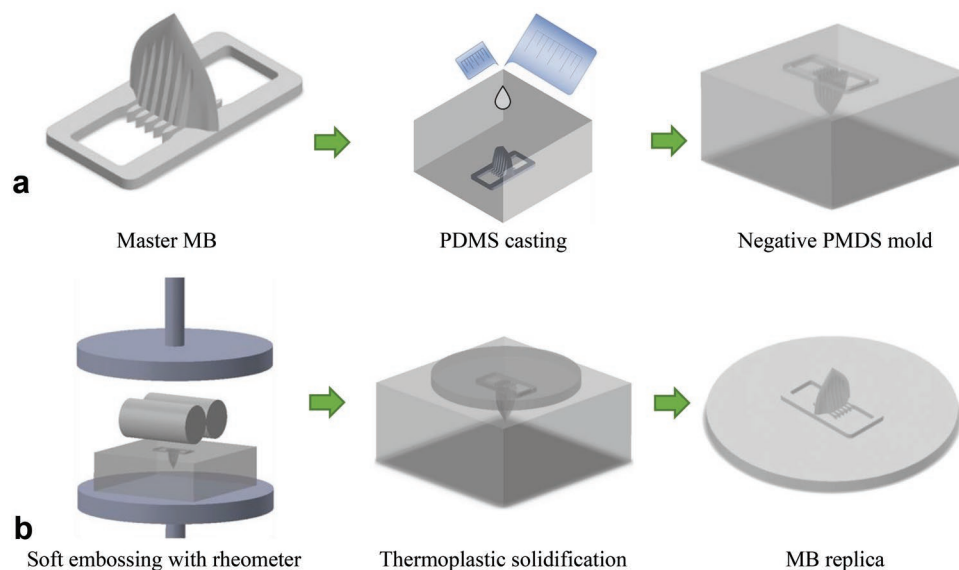
**ADVANCED
SCIENCE NEWS**
www.advancedsciencenews.com

**ADVANCED
MATERIALS
INTERFACES**
www.advmatinterfaces.de

Figure 2. Schematic representation of the polymer MB replication process, a) casting of negative PDMS mold from the master MB, b) soft embossing of the polymeric MB.

then processed using MATLAB (Natick, MA, USA) software to compare MBs' mechanical responses, including initial stiffness and failure points.

2.6. Scanning Electron Microscopy

The MB morphology and dimensions before and after compression testing were observed using a scanning electron microscope (SEM, JOEL JSM-7001F). Samples were attached to a metal stub using double-sided carbon tape. The stubs containing the MB samples were then coated with a 10 nm layer of platinum using JOEL Desktop Sputterer to avoid sample charges during SEM imaging. To study the MB tip size and angle, metal stubs with 90° angled holders capable of vertically mounting samples were used. The secondary electron detector with an accelerating voltage of 15 kV in high vacuum mode was used for SEM.

2.7. Manufacturing an Impact Applicator

A spring-loaded applicator prototype was designed in Solid-Works and printed using a Teirtime X5 3D printer (Teirtime Corporation, Milpitas, CA, USA) from PLA filaments to test the effect of application conditions. This applicator could adjust impact velocity and included a locking mechanism for activation. The design was consisted of three slots in the plunger and a top screw to regulate the impact velocity (**Figure 3**a). A high-speed camera (Photron Fastcam SA3), equipped with Nikon Nikkor 50 mm f 1.4 lens was used to measure the applicator impact velocities. During the test, the plunger was fixed by the locking mechanism, then released by pressing the push button from all three positions while motion images were captured at 4000 fps. The images were further analyzed using ImageJ (U. S. National Institutes of

Health, Bethesda, MD, USA) to determine the applicator's impact velocities. Figure 3b shows the stacked images at equally spaced time intervals to estimate the impact velocity of three different positions.

2.8. Skin Insertion and Diffusion Tests

The penetration efficiency and drug delivery of the MBs were tested using abdominal porcine cadaver skins.[34] Studies were performed using experimental procedures approved by the University of Southern Queensland (USQ) and the University of Queensland (UQ) animal ethics (Ethics Number: 20EXE005) and biosafety committees (Biosafety Number: 21BIOS003). Porcine cadaver skins were carefully shaved and cut into 3 ± 0.1 mm thick samples using a scalpel blade, and the fat layer underneath the hypodermis layer was removed. The tissue samples were then kept frozen at −20 °C and naturally thawed before the tests. The skin tissue was fixed by a custom-made skin stretching mechanism to control the skin strains (Figure S3, Supporting Information). The skin was gently stretched ≈5% from the original undeformed state to mimic the skin in vivo condition.[35]

Oxygen plasma treatment (Harrick Plasma Cleaner PDC-001, Harrick Plasma, Ithaca, NY, USA) was conducted for a minute with 30 W RF power on the MBs before the tests to increase the hydrophilicity of the MBs surface. Fluorescein was used as a model drug with 376.27 g mol^{-1} molecular weight (sodium salt, F6377, Sigma-Aldrich Corp., St. Louis, MO, USA). The concentrated aqueous solution was prepared from the mixture of fluorescein and deionized water (0.1% w/v). The tips of the MBs were dipped into a 0.1 µL droplet of the solution, enabling the flow through the channels into the reservoir by capillary flow. Fluorescence-coated MBs were then attached to the plunger of the prototype applicator with double-sided tape and applied to the abdominal porcine skin.
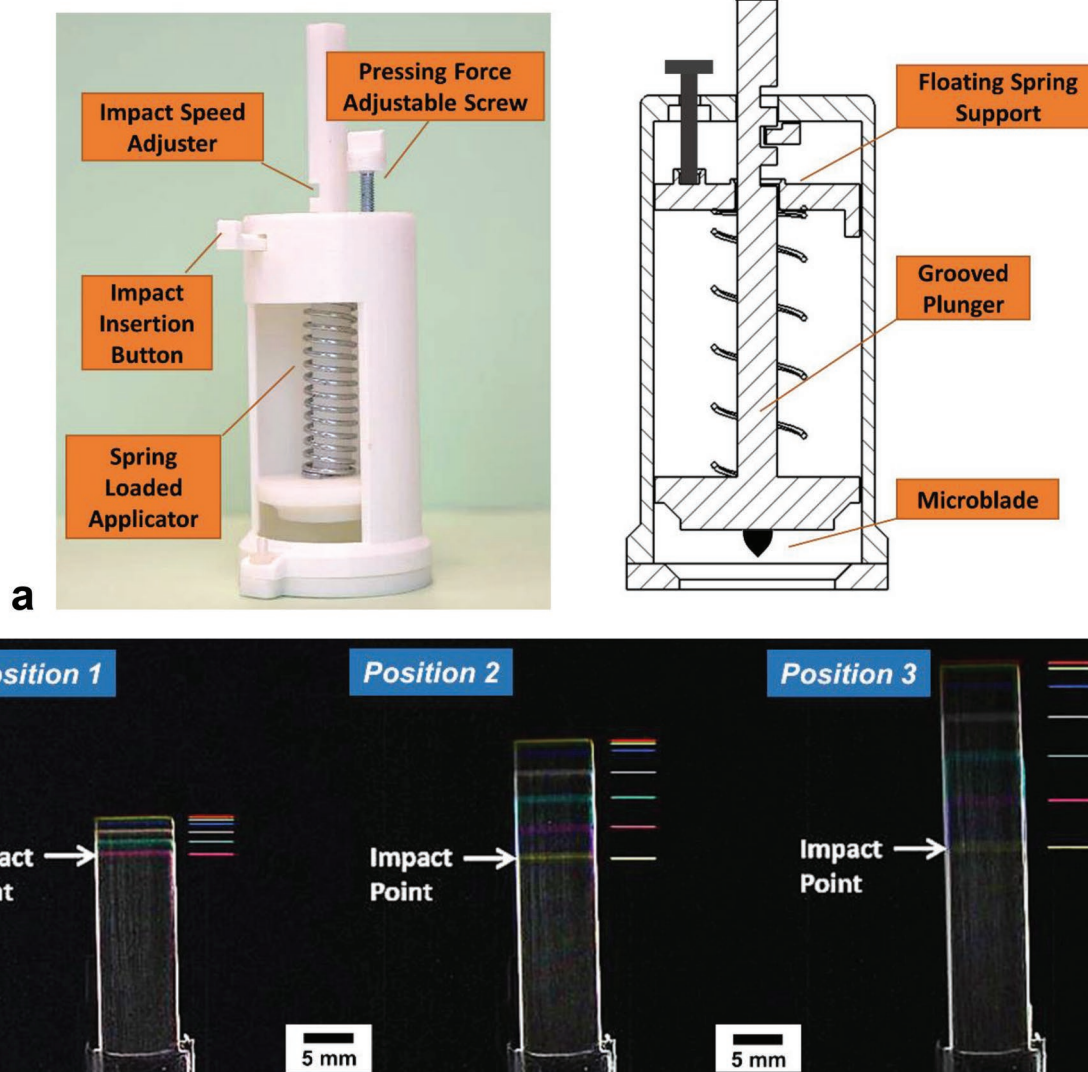
Figure 3. a) 3D-printed prototype applicator capable of adjusting impact velocity. b) High-speed camera images track the location of the plunger.

The first set of experiments was conducted with the insertion of all MB designs on the abdominal porcine skin with an impact velocity of 4.5 m s^{-1}. The second set of experiments was performed by inserting only the MB Type 1 on the skin tissue with impact velocities of 1.5, 3, and 4.5 m s^{-1}. After insertion, MBs were held on the skin surface for 5 min; upon removing the MBs from the skin tissues, the surface of the skin was tape stripped (20 ± 3 cycles) using 3 M Scotch Magic tape (3 M, USA) from different directions to remove the SC layer of the skin.[36,37] The penetration of fluorescein below the surface of the skin was visualized 20 min after each test by a confocal laser scanning microscope (CLSM, Zeiss LSM710, Germany) using Z-stack imaging with run times of 15 min.

2.9. Histology of MBs Penetration

Histology was used to confirm MBs penetration into the porcine skin. Sections were obtained using the cryosectioning technique. MB insertion sites were excised using scalpels, then placed upright into the cryostat mold, partially covered by optimal cutting temperature (OCT) compound (Tissue-Tek, Sakura Finetek, Torrance, USA). Once the skin sample was positioned inside the cryostat mold, the remaining mold cavities were filled by OCT and then frozen inside dry ice containers. Subsequently, the frozen specimens were sectioned into 50 µm thick slices using a Leica CM3050 cryostat (Leica Microsystems, Wetzlar, Germany) and placed on the Superfrost glass slides. The tissue sections were imaged by CLSM to visualize the MB penetration and diffusion of the model drug inside the skin.

2.10. FEA of MBs Insertion

A 3D planer symmetric finite element model was generated using the ANSYS (Canonsburg, PA, USA) explicit dynamics module to evaluate the MBs insertion mechanics into the skin.

**ADVANCED
SCIENCE NEWS**

www.advancedsciencenews.com

**ADVANCED
MATERIALS
INTERFACES**

www.advmatinterfaces.de

Table 2. Material parameters of the MB and the multilayered human skin model used in ANSYS explicit dynamics.

Parameter	Microblade	Stratum corneum	Dermis	Hypodermis
Mathematical model	Linear elastic	Linear elastic	Hyperelastic: Ogden 1st order	Linear elastic
Thickness [mm]	–	0.026	2	1.1
Young Modulus [MPa]	2100	28.4	–	0.1
Poisson ratio	0.48	0.49	0.49	0.48
Density [kg mm^{-3}]	1.01 E-6	1.3 E-6	1.2 E-6	9.71 E-7
Hyperelastic coefficients MU1, A1 [MPa]	–	–	0.0568, 13.3	–
Incompressibility factor [MPa^{-1}]	–	–	0.0745	–
Failure criteria [MPa]	–	20	7	–
Refs.	[38]	[39,40]	[40,41]	[40]

Skin models comprised three layers, SC, dermis, and hypodermis, with 26 µm, 2 mm, and 1.1 mm thicknesses, respectively. An Ogden (first-order) model with uniaxial test data was applied for the dermis layer, while SC and hypodermis were assumed to respond following a linear elastic model. Quadrilateral meshing with specific bias types, with factors of 3 to 4, was used to increase the number of elements near the MB–skin interfaces. FEA models calculated the insertion forces required to penetrate all MB types into the skin with a constant velocity of 4.5 m s^{-1} during insertion. Additionally, the FEA model calculated the penetration depth of all MBs with an initial velocity of 4.5 m s^{-1}, which was reduced upon insertion into the multilayered skin model. The material erosion method was used to enable MBs penetration into the skin model. The erosion algorithm eliminated the elements that reached the material failure point while retaining their inertia effect. **Table 2** summarizes the parameters used for the MBs and the multilayered skin models.

2.11. 3D Modeling of Drug Diffusion into Skin

A 3D simulation using COMSOL Multiphysics (COMSOL Multiphysics, COMSOL AB, Sweden) was used to model the diffusion of the fluorescein model drug into the skin. A two-layered skin model (SC and dermis) with negative cavity volumes representing fully penetrated individual MBs were initially created in SolidWorks. The 3D model was then imported to COMSOL Multiphysics to perform a series of time-dependent numerical simulations. The diffusion model incorporated nonconvection mass transport based on the time-dependent concentration of the model drug. The concentration decay function for the model drug was derived according to the Fick's second law of nonsteady-state diffusion (Equation (1))

$$\frac{\partial C}{\partial t} = D\left(\frac{\partial^2 C}{\partial x^2}\right) \tag{1}$$

where $\frac{\partial C}{\partial t}$ is the concentration rate and $\frac{\partial C}{\partial x}$ is the concentration gradient. Thus, the concentration $C_{(t)}$ on the MB surface was described by the decay function in Equation (2)[42]

$$C_{(t)} = C_0 + (C_s - C_0)\left(1 + \mathrm{erf}\left(\frac{x}{2\sqrt{Dt}}\right)\right) \tag{2}$$

where C_0 (mol m^{-3}) is the initial concentration of the model drug within the skin, C_s (mol m^{-3}) is the MB initial surface concentration, D (m^2 s^{-1}) is the diffusion coefficient, t is the time (s), and x is the skin thickness at the location of penetration (m). Based on the simulation setup, no initial drug concentration pre-existed in the skin ($C_0 = 0$), and a no flux condition was assumed for the skin boundaries. The dermal-subcutaneous junction (the boundary between the dermis layer and the subcutaneous fat layer beneath) was set to act as the sink condition of the model. A fluorescein model drug with an initial concentration of 2.66 (mol m^{-3}), along with diffusion coefficients of 3.97E-16 and 5.8E-10 m^2 s^{-1}, was used for the SC and dermis layers.[43,44] The simulation calculated the average concentrations (mol m^{-3}) of the model drug near the tip of the MB and at the bottom of the dermis layer (subcutaneous layer junction) within 20 min. Additionally, the concentration gradient of the model drug was calculated through the skin from the near tip to the end of the dermis layer.

2.12. Statistical Analysis

Experimental and simulation results were presented as the mean ± standard deviation ($n = 3$). Error bars were expressed as the standard deviations from the mean. For statistical comparisons, one-way analysis of variance (ANOVA) was used for insertion and penetration characteristics of all MBs (Types 1–5), and the p-value was set at < 0.05 for statistical significance. The statistical calculations were conducted using Office 365 Microsoft Excel (Microsoft Corporation, Redmond, WA, USA).

3. Results

3.1. Fabrication of MBs

Five types of complex master MBs were printed directly from CAD models using 2PP with submicron resolution. **Figure 4**a shows an MB replicated from its master fabricated using 2PP technique. Thermoplastic replicas of the masters were fabricated from the negative PDMS molds using soft embossing process with high spatial resolution. The negative PDMS molds of the masters were used for >20 cycles without any defect or impacting the overall quality and fidelity of the replicas. Replicated MBs had 849.29 ± 3.1 µm (mean ± SD; $n = 5$) overall height with ≈5.63% overall shrinkage from the masters. Figure 4b–f shows the SEM images of the MB replicas, and Figure 4g shows a typical tip of the MB Type 2 with a tip size of less than 5 µm.

**ADVANCED
SCIENCE NEWS**

www.advancedsciencenews.com

**ADVANCED
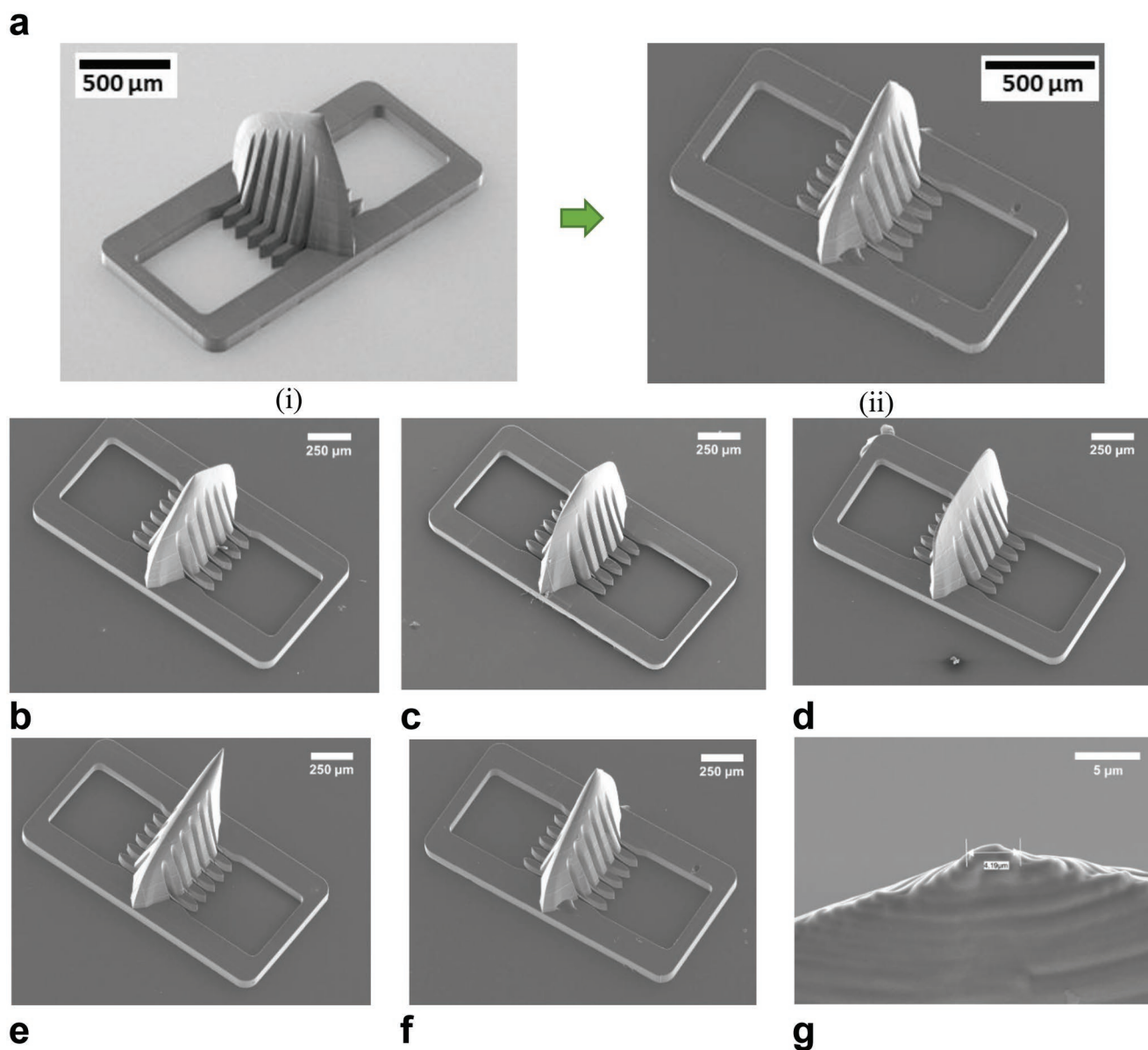MATERIALS
INTERFACES**

www.advmatinterfaces.de

Figure 4. a) Comparison of the i) master MB fabricated by 2PP versus ii) MB replica fabricated by soft embossing. SEM images of the MB replicas b) Type 1, c) Type 2, d) Type 3, e) Type 4, f) Type 5, and g) tip sharpness of the MB Type 2.

3.2. Mechanical Compression Testing of MBs

Compression tests were conducted at compression speeds of 1 and 25 μm s^{-1} to evaluate the insertion damage, initial stiffness, and failure points of each MB when a compressive force was applied along the vertical axis of the MB. **Figure 5**a–e shows the SEM images of the MBs after compression tests, where failure is defined by the deformation occurring close to the MB's tip by bending. Initial stiffness in the compression test can be defined as the slope in the linear region of the force–displacement graph, and failure points are the first occurrence of a sudden drop in the force–displacement graph, which leads to permanent deformation of the MB. Figure 5f,g shows the force–displacement graphs of the MBs

compression tests for 1 and 25 μm s^{-1} compression speeds. At the compression speed of 1 μm s^{-1}, the initial stiffness varied across MB Types 1–5 with values of 11.12, 13.22, 17.03, 8.78, and 2.71 N mm^{-1}, respectively. The trend remained the same for the 25 μm s^{-1} compression speed; however, due to the effects of strain rate on viscoelastic material response, the stiffness values increased to 22.10, 24.30, 29.98, 19.56, and 9.06 N mm^{-1} for Types 1–5, respectively. In both experiments, MB Type 3 showed the highest stiffness, whereas MBs Types 4 and 5 had the lowest stiffness. Effects of strain rate were also observed on failure points when the compression test speed increased from 1 to 25 μm s^{-1}. For instance, the failure point increased from 1.71 N at 1 μm s^{-1} to 5.43 N at 25 μm s^{-1} test speed for MB Type 3.

**ADVANCED
SCIENCE NEWS**

www.advancedsciencenews.com

**ADVANCED
MATERIALS
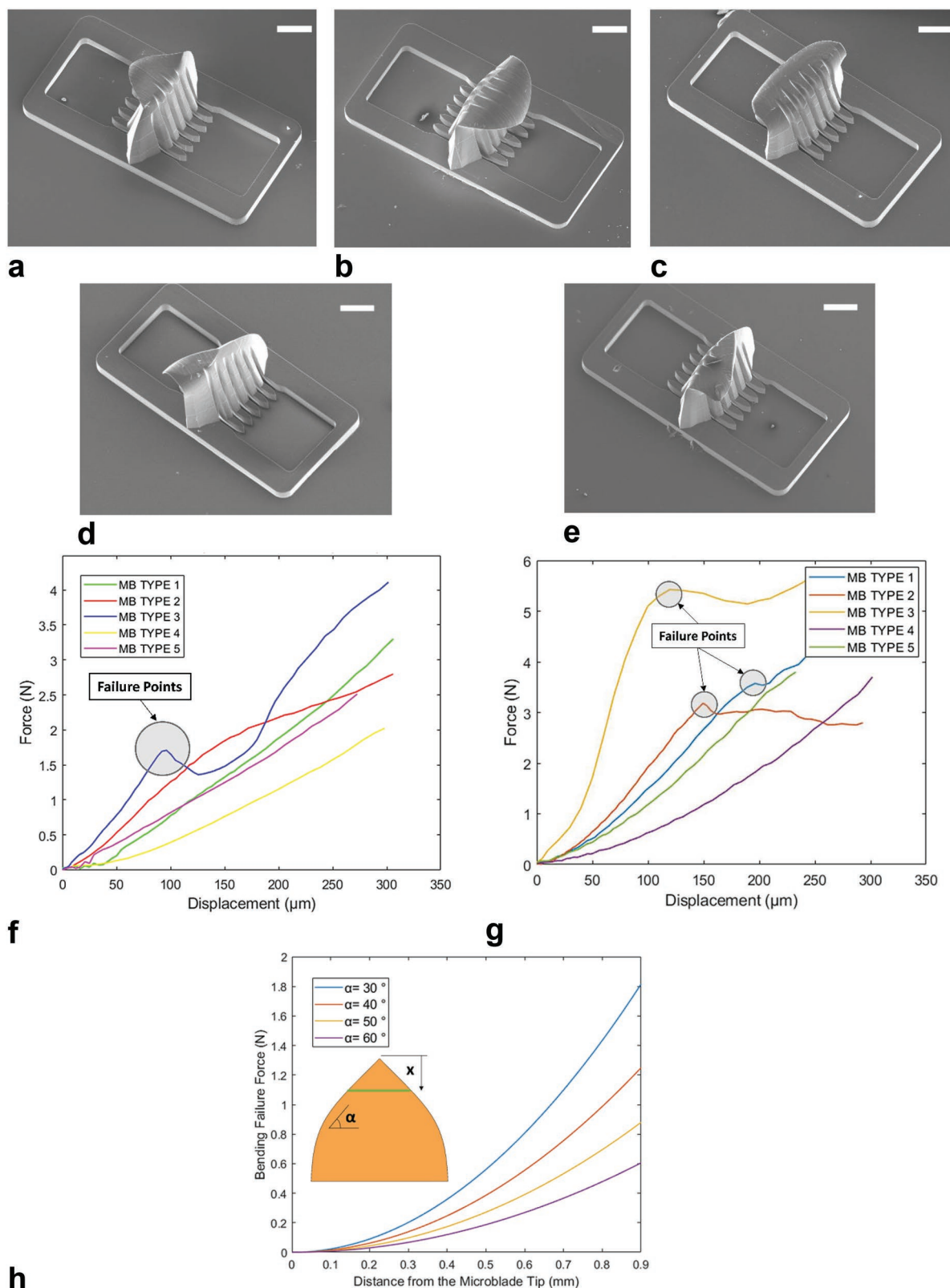INTERFACES**

www.advmatinterfaces.de

Figure 5. SEM images of MBs after mechanical compression tests for a) MB Type 1, b) MB Type 2, c) MB Type 3, d) MB Type 4, and e) MB Type 5 (scale bar = 200 μm). Force–displacement graphs of compression tests at f) 1 μm s^{-1} speed and g) at 25 μm s^{-1} speed for Types 1–5 of MBs. h) Theoretical representation of the critical failure bending load at different locations (x) from the MB tip based on varying MB tip angles (30° < α <60 °) with a constant side angle (β = 80°).

As evident from Figure 5a–e, bending is the primary mode of failure for MBs. In addition to experimental data, theoretical analysis can give an in-depth understanding of the effects of various factors on the overall MB mechanical integrity. During MB insertion, the skin elastic behavior and irregular topology impose axial and lateral loads on the microstructure that may result in different failure scenarios. The mathematical models assist in predicting the influence of geometrical parameters on MB bending, which is one of the most probable causes of MB failure. Assuming an MB acts as a cantilever beam with a point load perpendicular to the neutral axis, the varying second moment of inertia $I_{(x)}$ is determined in terms of the distance from the MB tip (x). The Euler–Bernoulli beam theory predicts a decrease in bending stress when moving toward the MB base. The critical bending load ($F_{bending}$) can be calculated using Equation (3)

$$F_{bending} = \frac{\pi \sigma_Y L^2}{4 \tan(\alpha) \tan^2(\beta)} \qquad (3)$$

where σ_y is the yield stress, L is the MB length, α and β represent the MB angles from either side (see Figure 1). The model predicts that the critical $F_{bending}$ is directly proportional to L and σ_y, while inversely proportional to α and β. According to this model, L and β parameters have the most influential effect on determining the critical $F_{bending}$. For a constant value of $\beta = 80°$, Figure 5h shows the critical $F_{bending}$ at different locations from the MB tip for side angles ranging from $30° < \alpha < 60°$.

3.3. Penetration and Delivery of Fluorescein into Skin

The penetration and drug delivery capabilities of the MBs were determined by measuring the penetration depth of fluorescein solution within the skin layers. A series of insertion tests ($n = 15$) were conducted on the porcine cadaver skin using the custom-made applicator with an impact velocity of 4.5 m s⁻¹ for all MB designs. To determine the depth of dye penetration, the Z-stacks imaging was conducted from the top surface of the MB-treated porcine skin with 10 μm intervals over 15 min for each test. **Figure 6**a shows the penetration and diffusion images of the fluorescein solution after insertion of an MB Type 1 to the tissue sample, taken from the top of the skin surface to ≈230 μm underneath the skin. The depth of penetration of each MB was determined based on the mean ± standard deviation (Figure 6b). In addition, fractional penetration length (FPL: percentage of MB penetrated length/overall MB length) was determined using the data from the Z-stack images. The results indicated that all Types 1–5 of MBs successfully penetrated the skin's SC layer having FPLs of 24.5 ± 5.32%, 23.78 ± 3.46%, 16.25 ± 4.3%, 26.59 ± 3.11%, 28.58 ± 7.28% (mean ± SD; $n = 3$), respectively (Figure 6c). According to the data (shown in Figures 6b,c), the Type 3 MB had the least penetration at 138 ± 36.51 μm with FPL of 16.25 ± 4.3%, and MB Types 4 and 5 had the furthest penetration achieving depths of 224.73 ± 26.42 μm (FPL: 26.59 ± 3.11%) and 242.63 ± 61.76 μm (FPL: 28.58 ± 7.28%).

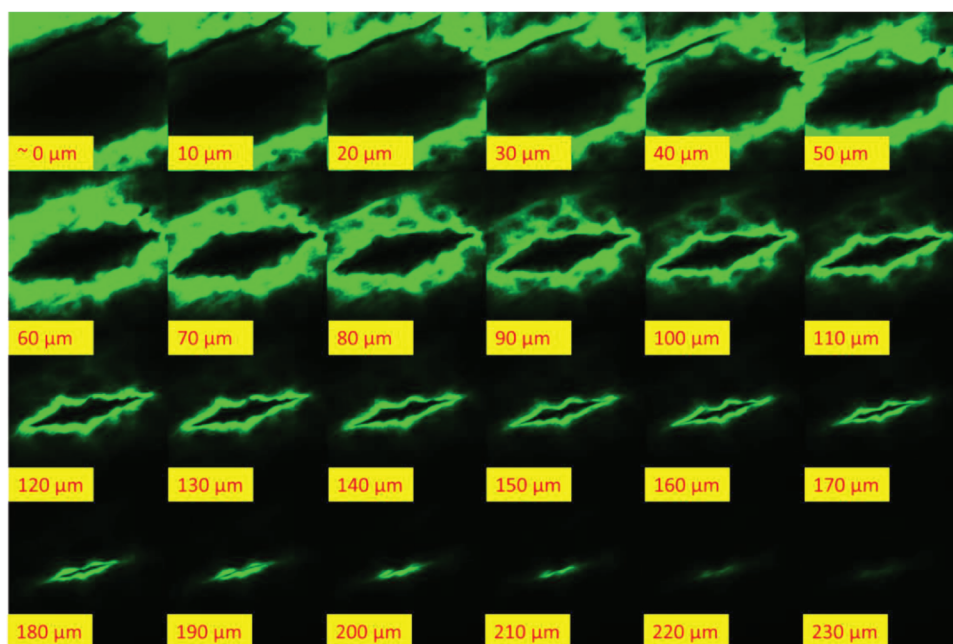In another experiment, the Type 1 MB was inserted in the abdominal porcine tissues using the applicator with impact velocities of 1.5, 3, and 4.5 m s⁻¹ to investigate the effect of impact velocity on penetration. The results show that increasing the impact velocity significantly increased the depth of penetration of this MB from 172 μm for 1.5 m s⁻¹ impact velocity to 196 and 254 μm for 3 and 4.5 m s⁻¹ impact velocities. This is equivalent to ≈45% increase in the overall penetration depth from 1.5 to 4.5 m s⁻¹ impact velocities (**Figure 7**a). Figure 7b shows the diffusion pattern of the fluorescein solution in the skin after applying an MB Type 1 at 4.5 m s⁻¹ impact velocity. As can be seen from Figure 7b, the 3D image resembled the MB's overall shape within the tissue. Histology studies for MB Type 2 also showed the skin penetration and diffusion pattern of the model drug deep into the skin epidermal layer (Figure 7c).
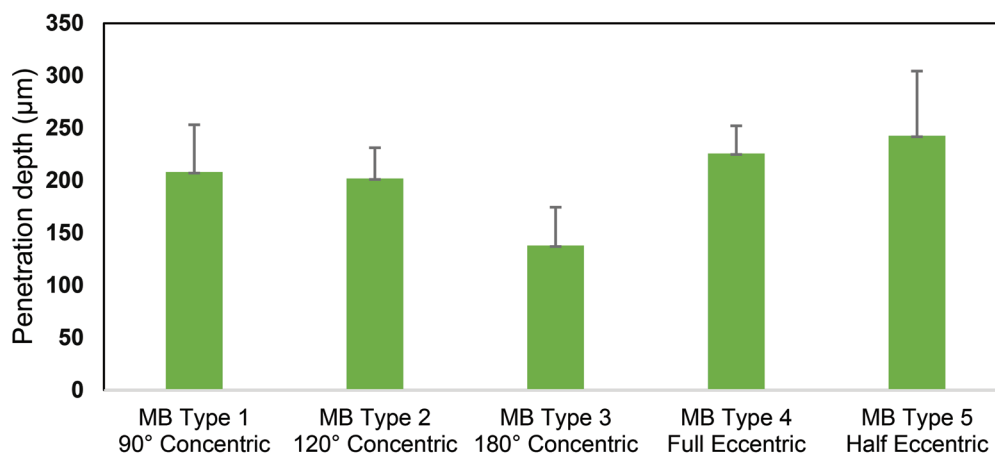
3.4. FEA of MB Insertion into Skin

The explicit dynamic module of ANSYS was used for FEA simulations (Video S1, Supporting Information). The skin was modeled as a multilayered model with a planner symmetry region combined with hyperelastic and linear elastic material properties. The boundary conditions of the model are indicated according to **Figure 8**a. The force of insertion and the penetration depth of MBs were calculated and plotted against their displacement into the skin model. The results indicated an increase in the force peaking at insertion before a drop as the skin was punctured. Figure 8b shows that the forces of insertion for Types 1–5 MBs were 0.1, 0.17, 0.52, 0.085, and 0.092 N. The Type 3 MB had the highest insertion force among all MBs, indicating that approximately five times more force is required to insert this design of the MB into the skin in comparison to the other designs. Figure 8c shows the insertion force of each MB design. In addition, penetration depth was determined during the FEA simulations of the MBs. Although the FEA results indicated a similar pattern to experiments, the results for penetration depth were smaller in FEA models. For Types 1–5 MBs, these penetration depths were 167.36, 155.70, 65.61, 198.74, and 169.18 μm, respectively. Results for MB penetration indicated that the Type 4 MB had the maximum penetration depth of 198.74 μm with FPL of 22.08%. Similar to the experiments, the Type 3 MB had a minimum penetration of 65.61 μm with FPL of 7.3%. Figure 8d shows the values of penetration depth obtained for five MB designs after insertion into the multilayered skin model.
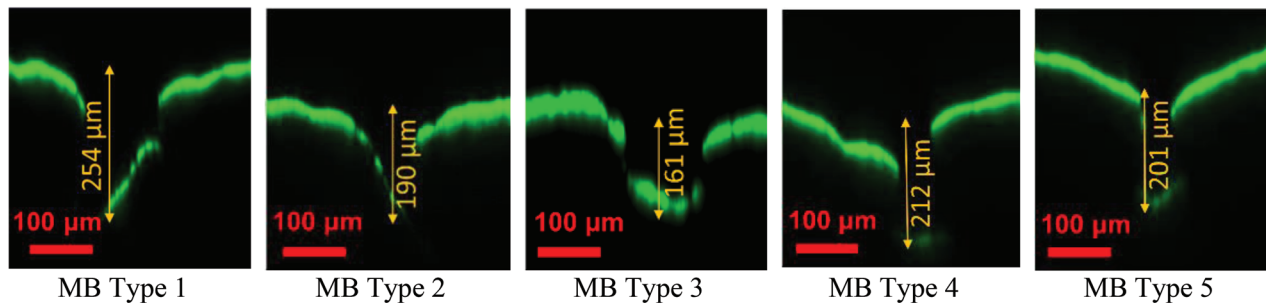
3.5. Drug Diffusion Modeling

COMSOL Multiphysics was used to simulate the diffusion of fluorescein as a drug through the multilayered skin model. **Figure 9**a shows the overall setup of the 3D model used for diffusion simulation of the model drug. This setup consisted of a two-layered skin model with no flux condition around the skin, a time-dependent MB concentration as described by Equation (2), and the data collection paths (1–3) (Figure 9a). The initial concentration of the drug in the skin model was assumed to be zero. Based on the simulation results, the concentration of the model drug significantly increased around the penetration

**ADVANCED
SCIENCE NEWS**

www.advancedsciencenews.com

**ADVANCED
MATERIALS
INTERFACES**

www.advmatinterfaces.de

Figure 6. a) Fluorescein solution diffusion underneath the porcine skin surface after application of a Type 1 MB with an impact velocity of 4.5 m s^{-1} illustrated from the skin surface to the deepest detectable fluorescein dye using confocal Z-stacks technique, b) penetration depth of five MB designs after insertion into the porcine abdominal skin with 4.5 m s^{-1} impact velocity, the data are expressed as mean ± SD ($n = 3$, $p < 0.1$; one-way ANOVA). c) Cross-sectional view of the tissues showing the maximum detectable penetration of Types 1–5 MBs, applied at a constant impact velocity of 4.5 m s^{-1}, having FPLs of 24.5 ± 5.32%, 23.78 ± 3.46%, 16.25 ± 4.3%, 26.59 ± 3.11%, 28.58 ± 7.28% (mean ± SD; $n = 3$), respectively.
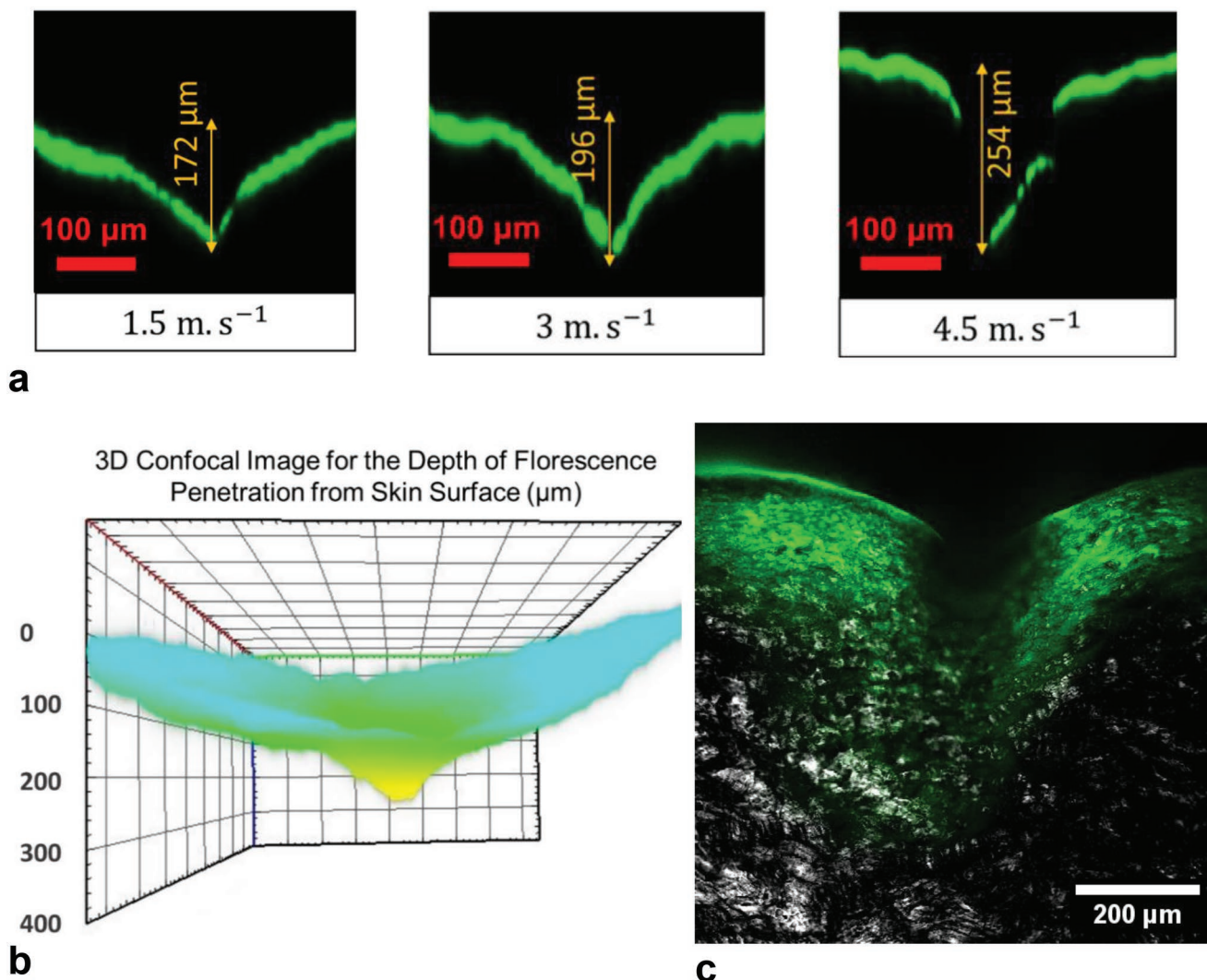
Figure 7. a) Cross-sectional view of the tissues showing the maximum detectable penetration of Type 1 MB, applied at impact velocities of 1.5, 3, and 4.5 m s^{-1}. b) 3D confocal image showing the penetration and diffusion of fluorescein dye underneath the skin's epidermal layer. c) The histology section for Type 2 MB illustrates skin penetration and the diffusion of fluorescein as a model drug deep into the skin's epidermal layer.

region in the first 5 min; however, the diffusion rate started to slow significantly after the first 12 min (Figure 9b) (Video S2, Supporting Information). The results from the simulation are presented as concentration profiles and streamlines (Figures 9c,d), demonstrating that the diffusion flux depends on the MB geometry. By increasing the tip angle from 90° to 180° (MB Types 1–3) the concentration gradient shifted toward the dermal-subcutaneous junction. Concentration gradients for eccentric MB Types 4 and 5 appeared to generate a nonuniform drug distribution (Figure 9d). After 20 min, for MB Types 1–5, a concentration of 1.07, 1.15, 1.37, 1.05, and 1.06 mol m^{-3} was achieved near the tip of each MB. Thus, the maximum concentration of 1.37 mol m^{-3} was noted for MB Type 3, while MB Types 1, 4, and 5 had the least concentration of ≈1.05 mol m^{-3}. At the near subcutaneous layer, concentrations of 0.49, 0.51, 0.57, 0.5, 0.5 mol m^{-3} were observed for MB Types 1–5. Again, for MB Types 1, 4, and 5, which have a similar tip shape and angle, a lower drug concentration was observed near the

subcutaneous layer. Figure 9e shows the average fluorescein concentration at the two locations (near MB tip and subcutaneous layer) for each MB, and Figure 9f shows the fluorescein concentration gradient across the skin thickness.

4. Discussion

In this study, complex microstructures were created directly from CAD drawing using the 2PP technique and replicated using PDMS micromolding and soft embossing methods. These fabrication methods allow the production of complex MBs with good repeatability and high mechanical strength, which are not achievable by other micro-manufacturing processes. 2PP is the most versatile method for manufacturing microstructures, especially MNs and MBs.[8] Our previous studies demonstrated the fabrication of complex MN arrays using 2PP techniques.[9,38] Similar to MNs, MBs need
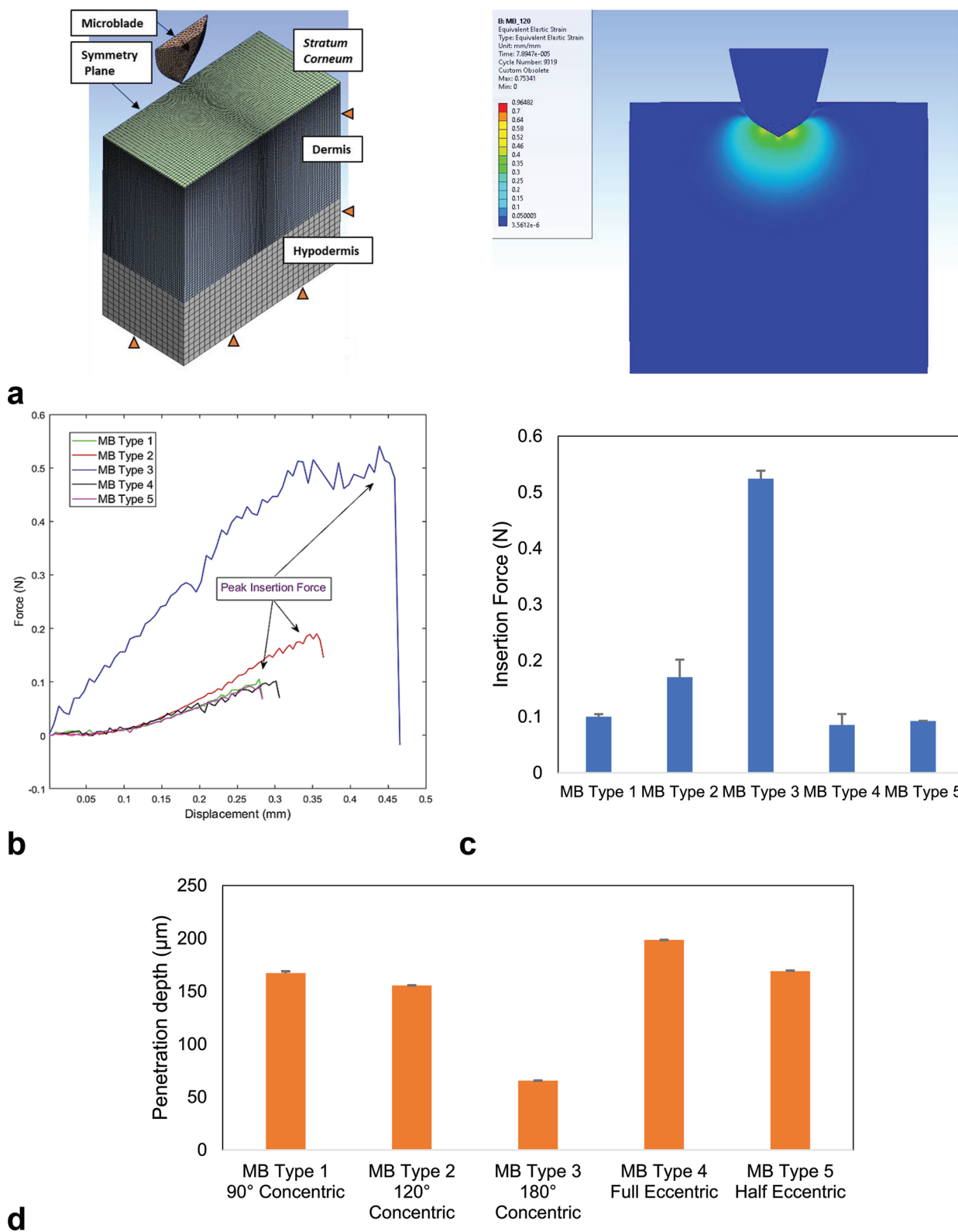
ADVANCED
SCIENCE NEWS

www.advancedsciencenews.com

ADVANCED
MATERIALS
INTERFACES

www.advmatinterfaces.de

Figure 8. a) Boundary conditions and quadrilateral bias meshing used for FEA of the MBs, showing SC, dermis, and hypodermis layers. b) Calculation of peak insertion force before MBs pierce the SC layer of the skin model. c) Bar chart showing the insertion force achieved from the simulation of the MBs during insertion into the skin model with a velocity of 4.5 m s^{-1}. The data are expressed as mean ± SD (n = 3, p < 0.001; one-way ANOVA). d) Penetration depth was achieved from the simulation of the MBs during insertion into the skin model with a velocity of 4.5 m s^{-1}. The data are presented as mean ± SD (n = 3, p < 0.001; one-way ANOVA).

**ADVANCED
SCIENCE NEWS**

www.advancedsciencenews.com

**ADVANCED
MATERIALS
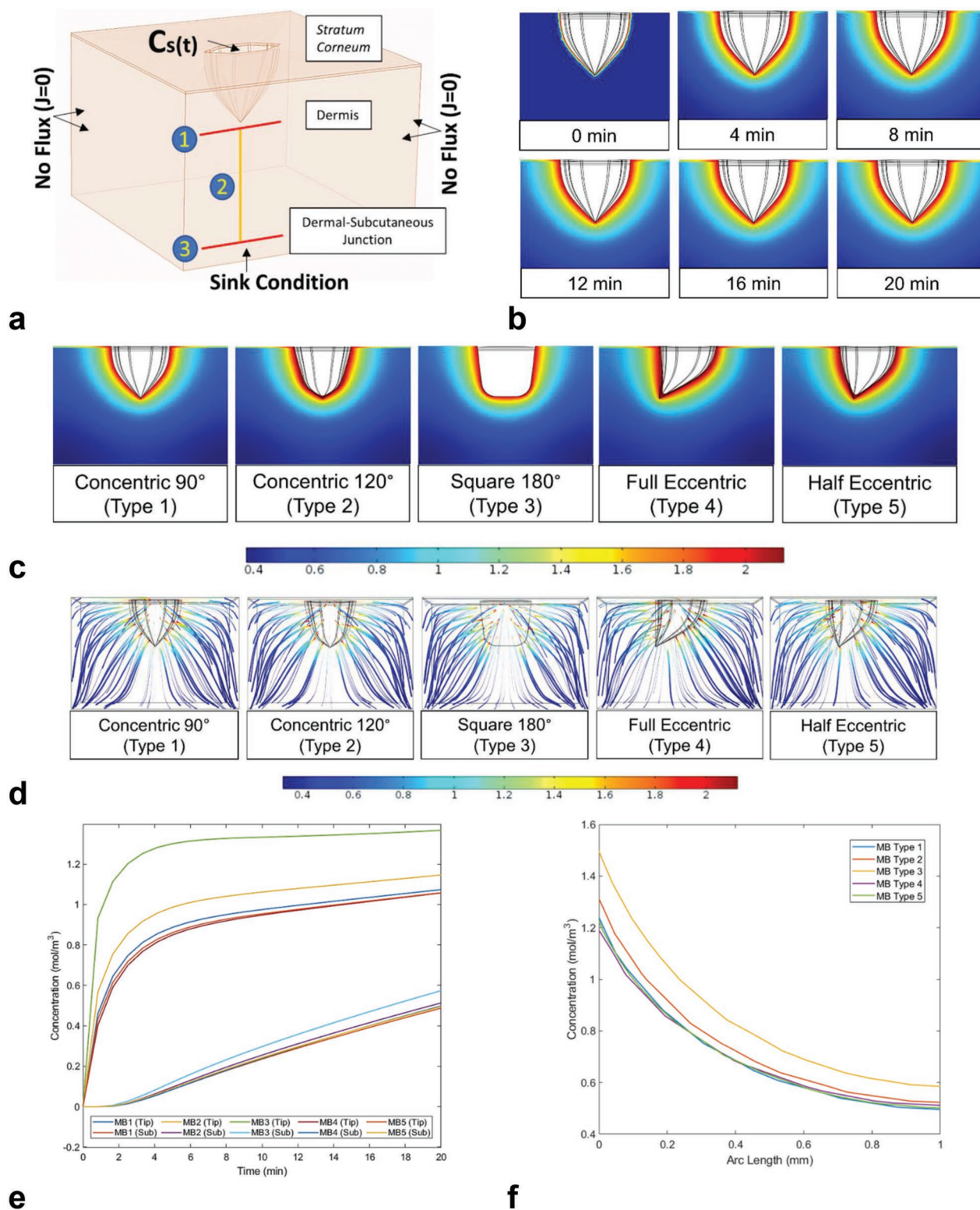INTERFACES**

www.advmatinterfaces.de

Figure 9. a) The simulation setup for the diffusion model consists of time-dependent concentration, no flux boundary condition, and measurement lines for data collection. Model drug concentrations on lines 1 and 3 are averaged at different time intervals, while line 2 represents the concentration gradient through the skin underneath the penetration region. b) Concentration profile for MB Type 1 at different time intervals 0, 4, 8, 12, 16, and 20 min. c) Fluorescein concentration profile of all five MBs at 20 min. d) Color-coded concentration gradient streamlines showing the diffusion of the model drug after 20 min across the skin thickness for five MBs. e) Average fluorescein concentration (mol m^{-3}) versus time (min) at two locations (near MB tip and at subcutaneous layer). f) Concentration (mol m^{-3}) versus arc length (mm) extended from MB tip to subcutaneous layer.

**ADVANCED
SCIENCE NEWS**

www.advancedsciencenews.com

**ADVANCED
MATERIALS
INTERFACES**

www.advmatinterfaces.de

sufficient strength to safely and reliably insert into the skin.[45] To improve the MB integrity and reduce the 2PP fabrication time, a series of process optimizations were conducted on the main printing parameters such as laser power, scanning speed, slicing distance, scaffolding method, and block size to select the most optimum set of parameters,[38,46] and print rigid microstructures with high durability. PDMS micromolding is a well-known technique to replicate microstructure. In this study, we used PDMS mold for soft embossing of a complete microfluidic device, including MB structure with open fluidic channels and reservoirs in a single embossing step. The reservoirs and fluidic channels are integrated into the design of the MBs to store and enable the transfer of fluids in and out of the skin. PDMS molds produced from master MBs were reused for several cycles without damage (>20). The axial force applied during the soft embossing process was carefully controlled to enable fabrication of high-precision replicas while avoiding microcracks to the PDMS mold. The maximum allowable pressure on the mold was adjusted based on the microstructures' geometrical complexity and the volume of thermoplastic materials required per replication cycle. Our previous study used lower pressure to replicate MN arrays,[38] which indicates the dependence of the applied force on the design geometries and the mold structure.

Axial compression tests were conducted at 1 and 25 μm s^{-1} compression speeds to evaluate the mechanical strength of the MBs. The data indicate an increase in mechanical strength upon the increase in the compression speed, i.e., faster insertion of MBs into the skin decreases the chances of early failure of MBs. During the tests, bending failures were observed (Figure 5), deemed the critical limitation to successful MB insertion.[47]

In this study, we demonstrated the successful insertion of MBs into the dermal layer with our customized applicator equipped with variable impact velocities. All the MB replicas ($n = 22$) successfully penetrated the skin with no breakage or separation, leaving no residue on the skin (Figure S4, Supporting Information). Enhancing the MB penetration can improve the drug delivery and sampling for diagnostics,[48,49] while reducing the fabrication costs associated with partial penetrations. As opposed to manual applications, using an applicator will assure the patient or carer that enough force has been applied to insert the MBs into the skin. In addition, increasing the impact velocity (and hence the strain rate) has remarkably improved the penetration.[48,50] Our results showed that increasing impact velocity from 1.5 to 4.5 m s^{-1} resulted in up to 45% increase in the overall FPL. According to the data, reducing the MB angle and introducing eccentricity in the design also improved the MBs' FPL. For a constant MB height and base size, the effects of eccentricity can be interpreted as a reduction in the MB angle as eccentricity increases from the center toward the sides. The effect of impact application on MN penetration has also been demonstrated in the literature.[48,51,52] Maaden et al. showed 40% lower MN array penetration efficiency and reproducibility when manual insertion was used over an impact insertion.[53] In another study, Meliga et al. showed that by increasing the impact velocity from ≈0.25 to 2 m s^{-1} a profound penetration depth enhancement from ≈20% to 60% was achieved.[50] In addition, through a series of simulations in ANSYS explicit dynamics, the insertion force required

to penetrate the skin for various MB designs was calculated. Insertion forces varied between 0.085 and 0.52 N depending on the MB overall geometrical shapes. These insertion force data were in accordance with the experimental results.

The diffusion pattern from the simulation of the drug model was comparable with the permeability studies using confocal imaging, with a steep decline in the concentration and diffusion flux over time. This diffusion pattern can be described based on the Fick's first law of diffusion (Equation (4))

$$J = -D\frac{\partial C}{\partial x} \qquad (4)$$

where J is the diffusion flux (mol m^{-2} s^{-1}), D is the drug diffusivity (m^2 s^{-1}) in skin, and $\frac{\partial C}{\partial x}$ (mol m^{-4}) is the concentration gradient. The rate of decrease in the concentration over time $\frac{\partial C}{\partial t} < 0$ (Equation 2), reduced both $\frac{\partial C}{\partial x}$ and the diffusion flux (J). At equal penetration depths, MB Types 2 and 3 showed the highest diffusion compared to other counterparts. The simulation data showed a 27.3% higher drug concentration near the MB Type 3 tip which was the highest concentration among concentric MBs. At the subcutaneous junction, this increase in concentration was less noticeable (17.7%). Uniformity and homogeneity of concentration are important factors in therapeutic drug delivery,[54] whereas in the current study introducing eccentricity to MBs Types 4 and 5 led to an uneven distribution of the model drug. Al-Qallaf et al. also previously reported the effects of MN nonsymmetrical features on drug distribution behavior.[54] Moreover, using fluorescein as a drug model with a molecular weight (MW) of 376.27 gr mol^{-1} can possess similar diffusivity compared to other FDA-approved drugs for transdermal delivery, such as Fentanyl (MW: 336.47 gr mol^{-1}), Oxybutynin (MW: 357.49 gr mol^{-1}), Donepezil (MW: 379.49 gr mol^{-1}) with comparable molecular weights.[55]

5. Conclusion

Microdevices such as MN and MB arrays are becoming promising means of drug delivery and sampling. In this research, a scalable manufacturing process[56] was used to fabricate MBs offering single integrated designs, which may reduce the fabrication cost and time while promoting safe and effective insertion into the skin subjects. MBs are a new design of MNs for transdermal drug delivery. Different geometries of MB were designed and fabricated using 2PP. Master MBs were then reproduced using micromolding and embossing processes.

Experiments were conducted to test the penetration capabilities by mounting MBs on prototype impact applicators and placing porcine abdomen cadaver skin on an adjustable stretching mechanism.[57] MB insertion simulations were carried out on a combination of hyperelastic and linear elastic multilayered skin models for individual MB designs to determine the insertion force and penetration capabilities. All MBs successfully penetrated through the skin SC layer, and a reduction in blade angle for concentric models and introduction of eccentricity to the MB overall shape was found to

increase the penetration. The simulation of model drug diffusion conducted across all MBs indicated a steep decline in the diffusion flux over time for solid MBs. While increasing the tip angle improved the concentration, eccentricity resulted in nonuniform concentration distribution. In terms of penetration, approximately a 45% increase was observed in penetration depth upon increasing the impact velocity by a factor of three. The results demonstrate the functional capabilities and potential for future applications of MBs for transdermal drug delivery.

Supporting Information

Supporting Information is available from the Wiley Online Library or from the author.

Conflict of Interest

The authors declare no conflict of interest.

Data Availability Statement

The data that support the findings of this study are available from the corresponding author upon reasonable request.

[1] R. S. J. Ingrole, E. Azizoglu, M. Dul, J. C. Birchall, H. S. Gill, M. R. Prausnitz, *Biomaterials* **2021**, *267*, 120491.

[2] S. A. Ranamukhaarachchi, B. Stoeber, *Biomed. Microdevices* **2019**, *21*, 100.

[3] R. V. Dixon, E. Skaria, W. M. Lau, P. Manning, M. A. Birch-Machin, S. M. Moghimi, K. W. Ng, *Acta Pharm. Sin. B* **2021**, *11*, 2344.

[4] E. Larrañeta, R. E. M. Lutton, A. D. Woolfson, R. F. Donnelly, *Mater. Sci. Eng., R* **2016**, *104*, 1.

[5] Z. Faraji Rad, P. D. Prewett, G. J. Davies, *Beilstein J. Nanotechnol.* **2021**, *12*, 1034.

[6] T. M. Tuan-Mahmood, M. T. McCrudden, B. M. Torrisi, E. McAlister, M. J. Garland, T. R. Singh, R. F. Donnelly, *Eur. J. Pharm. Sci.* **2013**, *50*, 623.

[7] S. Indermun, R. Luttge, Y. E. Choonara, P. Kumar, L. C. du Toit, G. Modi, V. Pillay, *J. Controlled Release* **2014**, *185*, 130.

[8] Z. Faraji Rad, P. D. Prewett, G. J. Davies, *Microsyst. Nanoeng.* **2021**, *7*, 71.

[9] Z. Faraji Rad, P. D. Prewett, G. J. Davies, *Manuf. Lett.* **2021**, *30*, 39.

[10] F. K. Aldawood, A. Andar, S. Desai, *Polymers* **2021**, *13*, 2815.

[11] J. H. Jung, S. G. Jin, *J. Pharm. Invest.* **2021**, *51*, 503.

[12] A. Tucak, M. Sirbubalo, L. Hindija, O. Rahic, J. Hadziabdic, K. Muhamedagic, A. Cekic, E. Vranic, *Micromachines* **2020**, *11*, 961.

[13] S. Khan, A. Hasan, F. Attar, M. M. N. Babadaei, H. A. Zeinabad, M. Salehi, M. Alizadeh, M. Hassan, H. Derakhshankhah, M. R. Hamblin, Q. Bai, M. Sharifi, M. Falahati, T. L. M. Ten Hagen, *J. Controlled Release* **2021**, *338*, 341.

[14] A. R. Johnson, A. T. Procopio, *3D Print. Med.* **2019**, *5*, 2.

[15] V. Ebrahiminejad, P. D. Prewett, G. J. Davies, Z. Faraji Rad, *Adv. Mater. Interfaces* **2022**, *9*, 2101856.

[16] J. H. Park, M. G. Allen, M. R. Prausnitz, *J. Controlled Release* **2005**, *104*, 51.

[17] J. Zhu, X. Zhou, H. J. Kim, M. Qu, X. Jiang, K. Lee, L. Ren, Q. Wu, C. Wang, X. Zhu, P. Tebon, S. Zhang, J. Lee, N. Ashammakhi, S. Ahadian, M. R. Dokmeci, W. Gu, W. Sun, A. Khademhosseini, *Small* **2020**, *16*, 1905910.

[18] S. Lin, G. Quan, A. Hou, P. Yang, T. Peng, Y. Gu, W. Qin, R. Liu, X. Ma, X. Pan, H. Liu, L. Wang, C. Wu, *J. Controlled Release* **2019**, *306*, 69.

[19] S. Dottermusch, D. Busko, M. Langenhorst, U. W. Paetzold, B. S. Richards, *Opt. Lett.* **2019**, *44*, 29.

[20] M. J. Uddin, N. Scoutaris, S. N. Economidou, C. Giraud, B. Z. Chowdhry, R. F. Donnelly, D. Douroumis, *Mater. Sci. Eng., C* **2020**, *107*, 110248.

[21] S. D. Gittard, B. Chen, H. Xu, A. Ovsianikov, B. N. Chichkov, N. A. Monteiro-Riviere, R. J. Narayan, *J. Adhes. Sci. Technol.* **2013**, *27*, 227.

[22] M. L. Crichton, C. Archer-Jones, S. Meliga, G. Edwards, D. Martin, H. Huang, M. A. F. Kendall, *Acta Biomater.* **2016**, *36*, 186.

[23] E. Z. Loizidou, N. T. Inoue, J. Ashton-Barnett, D. A. Barrow, C. J. Allender, *Eur. J. Pharm. Biopharm.* **2016**, *107*, 1.

[24] S. P. Davis, B. J. Landis, Z. H. Adams, M. G. Allen, M. R. Prausnitz, *J. Biomech.* **2004**, *37*, 1155.

[25] H. S. Gill, M. R. Prausnitz, *J. Controlled Release* **2007**, *117*, 227.

[26] G. Ma, C. Wu, *J. Controlled Release* **2017**, *251*, 11.

[27] P. P. Samant, M. R. Prausnitz, *Proc. Natl. Acad. Sci. USA* **2018**, *115*, 4583.

[28] M. Sausse Lhernould, C. Gobillon, P. Lambert, *ONdrugDelivery* **2013**, *40*, 29.

[29] P. Khanna, K. Luongo, J. A. Strom, S. Bhansali, *J. Micromech. Microeng.* **2010**, *20*, 045011.

[30] M. Leone, B. H. van Oorschot, M. R. Nejadnik, A. Bocchino, M. Rosato, G. Kersten, C. O'Mahony, J. Bouwstra, K. van der Maaden, *Pharmaceutics* **2018**, *10*, 211.

[31] H. B. Song, K. J. Lee, I. H. Seo, J. Y. Lee, S. M. Lee, J. H. Kim, J. H. Kim, W. Ryu, *J. Controlled Release* **2015**, *209*, 272.

[32] O. Olatunji, D. B. Das, M. J. Garland, L. Belaid, R. F. Donnelly, *J. Pharm. Sci.* **2013**, *102*, 1209.

[33] Z. Faraji Rad, R. E. Nordon, G. J. Davies, C. J. Anthony, P. Prewett, (NewSouth Innovations Pty Ltd, University of Birmingham), *US Patent 10850082*, **2020**.

[34] S. A. Ranamukhaarachchi, S. Lehnert, S. L. Ranamukhaarachchi, L. Sprenger, T. Schneider, I. Mansoor, K. Rai, U. O. Hafeli, B. Stoeber, *Sci. Rep.* **2016**, *6*, 32074.

2201115 (15 of 16)

ADVANCED
SCIENCE NEWS

www.advancedsciencenews.com

ADVANCED
MATERIALS
INTERFACES

www.advmatinterfaces.de

[35] H. V. Tran, F. Charleux, M. Rachik, A. Ehrlacher, M. C. Ho Ba Tho, *Comput. Methods Biomech. Biomed. Eng.* **2007**, *10*, 401.

[36] R. F. Donnelly, T. R. Singh, M. M. Tunney, D. I. Morrow, P. A. McCarron, C. O'Mahony, A. D. Woolfson, *Pharm. Res.* **2009**, *26*, 2513.

[37] P. Anantaworasakul, W. Chaiyana, B. B. Michniak-Kohn, W. Rungseevijitprapa, C. Ampasavate, *Pharmaceutics* **2020**, *12*, 463.

[38] Z. Faraji Rad, R. E. Nordon, C. J. Anthony, L. Bilston, P. D. Prewett, J. Y. Arns, C. H. Arns, L. Zhang, G. J. Davies, *Microsyst. Nanoeng.* **2017**, *3*, 17034.

[39] K. Levi, R. J. Weber, J. Q. Do, R. H. Dauskardt, *Int. J. Cosmet. Sci.* **2010**, *32*, 276.

[40] W. Shu, H. Heimark, N. Bertollo, D. J. Tobin, E. D. O'Cearbhaill, A. N. Annaidh, *Acta Biomater.* **2021**, *135*, 403.

[41] F. H. Silver, G. P. Seehra, J. W. Freeman, D. DeVore, *J. Appl. Polym. Sci.* **2002**, *86*, 1978.

[42] P. Shewmon, *Diffusion in Solids*, 2 ed., Springer, Cham, Switzerland **2016**.

[43] A. Göpferich, G. Lee, *Int. J. Pharm.* **1991**, *71*, 245.

[44] M. P. di Cagno, F. Clarelli, J. Våbenø, C. Lesley, S. D. Rahman, J. Cauzzo, E. Franceschinis, N. Realdon, P. C. Stein, *Mol. Pharmaceutics* **2018**, *15*, 1488.

[45] M. C. Chen, M. H. Ling, K. Y. Lai, E. Pramudityo, *Biomacromolecules* **2012**, *13*, 4022.

[46] A. S. Cordeiro, I. A. Tekko, M. H. Jomaa, L. Vora, E. McAlister, F. Volpe-Zanutto, M. Nethery, P. T. Baine, N. Mitchell, D. W. McNeill, R. F. Donnelly, *Pharm. Res.* **2020**, *37*, 174.

[47] J. W. Lee, J. H. Park, M. R. Prausnitz, *Biomaterials* **2008**, *29*, 2113.

[48] M. L. Crichton, A. Ansaldo, X. Chen, T. W. Prow, G. J. Fernando, M. A. Kendall, *Biomaterials* **2010**, *31*, 4562.

[49] T. M. Blicharz, P. Gong, B. M. Bunner, L. L. Chu, K. M. Leonard, J. A. Wakefield, R. E. Williams, M. Dadgar, C. A. Tagliabue, R. El Khaja, S. L. Marlin, R. Haghgooie, S. P. Davis, D. E. Chickering, H. Bernstein, *Nat. Biomed. Eng.* **2018**, *2*, 151.

[50] S. C. Meliga, J. W. Coffey, M. L. Crichton, C. Flaim, M. Veidt, M. A. F. Kendall, *Acta Biomater.* **2017**, *48*, 341.

[51] F. J. Verbaan, S. M. Bal, D. J. van den Berg, W. H. Groenink, H. Verpoorten, R. Luttge, J. A. Bouwstra, *J. Controlled Release* **2007**, *117*, 238.

[52] F. J. Verbaan, S. M. Bal, D. J. van den Berg, J. A. Dijksman, M. van Hecke, H. Verpoorten, A. van den Berg, R. Luttge, J. A. Bouwstra, *J. Controlled Release* **2008**, *128*, 80.

[53] K. van der Maaden, E. Sekerdag, W. Jiskoot, J. Bouwstra, *AAPS J.* **2014**, *16*, 681.

[54] B. Al-Qallaf, D. B. Das, A. Davidson, *Asia-Pac. J. Chem. Eng.* **2009**, *4*, 845.

[55] D. S. Wishart, Y. D. Feunang, A. C. Guo, E. J. Lo, A. Marcu, J. R. Grant, T. Sajed, D. Johnson, C. Li, Z. Sayeeda, N. Assempour, I. Iynkkaran, Y. Liu, A. Maciejewski, N. Gale, A. Wilson, L. Chin, R. Cummings, D. Le, A. Pon, C. Knox, M. Wilson, *Nucleic Acids Res.* **2018**, *46*, D1074.

[56] Z. Faraji Rad, P. D. Prewett, G. J. Davies, *Addit. Manuf.* **2022**, *56*, 102953.

[57] V. Ebrahiminejad, Z. Faraji Rad, P. D. Prewett, G. J. Davies, *Beilstein J. Nanotechnol.* **2022**, *13*, 629.